

# Zernike Phase Plate Cryoelectron Microscopy Facilitates Single Particle Analysis of Unstained Asymmetric Protein Complexes

Wei-Hau Chang,<sup>1,2,\*</sup> Michael T.-K. Chiu,<sup>1</sup> Chin-Yu Chen,<sup>1</sup> Chi-Fu Yen,<sup>1</sup> Yen-Cheng Lin,<sup>1</sup> Yi-Ping Weng,<sup>1</sup> Ji-Chau Chang,<sup>1,2</sup> Yi-Min Wu,<sup>1</sup> Holland Cheng,<sup>3</sup> Jianhua Fu,<sup>4</sup> and I-Ping Tu<sup>5</sup>

<sup>1</sup>Institute of Chemistry, Academia Sinica, Taipei, 115, Taiwan

<sup>2</sup>Department of Biochemical Sciences and Technology, National Taiwan University, Taipei, 106, Taiwan

<sup>3</sup>Department of Molecular and Cellular Biology, University of California, Davis, Davis, CA 95616, USA

<sup>4</sup>Department of Biochemistry, Medical College of Wisconsin, Milwaukee, WI 53226, USA

<sup>5</sup>Institute of Statistical Sciences, Academia Sinica, Taipei, 115, Taiwan

\*Correspondence: [weihau40@gmail.com](mailto:weihau40@gmail.com)

DOI 10.1016/j.str.2009.12.001

## SUMMARY

Single particle reconstruction from cryoelectron microscopy images, though emerging as a powerful means in structural biology, is faced with challenges as applied to asymmetric proteins smaller than megadaltons due to low contrast. Zernike phase plate can improve the contrast by restoring the microscope contrast transfer function. Here, by exploiting simulated Zernike and conventional defocused cryoelectron microscope images with noise characteristics comparable to those of experimental data, we quantified the efficiencies of the steps in single particle analysis of ice-embedded RNA polymerase II (500 kDa), transferrin receptor complex (290 kDa), and T7 RNA polymerase lysozyme (100 kDa). Our results show Zernike phase plate imaging is more effective as to particle identification and also sorting of orientations, conformations, and compositions. Moreover, our analysis on image alignment indicates that Zernike phase plate can, in principle, reduce the number of particles required to attain near atomic resolution by 10–100 fold for proteins between 100 kDa and 500 kDa.

## INTRODUCTION

Low-temperature bright-field transmission electron microscopy (cryo-EM) has emerged as a powerful tool in structural biology. Fourier synthesis of cryo-EM data of symmetric biological assemblies in hydrated state has led to three-dimensional atomic models (Gonen et al., 2005; Henderson et al., 1990; Unwin, 2005; Yonekura et al., 2003), while single-particle analysis (Frank, 2002, 2006; van Heel et al., 2000) of amorphous ice-embedded molecules (Adrian et al., 1984) of low or no symmetry allows the structures of various functional states to be determined to subnanometer resolution (Frank et al., 2007; Clare et al., 2009). As the discovery of protein complexes is spurred by affinity purification-assisted mass spectroscopy

(Gavin et al., 2002), structural proteomics of protein complexes has become an important subject (Sali, 2003). The fragility or scarcity of most protein complexes makes them refractory to crystallographic analysis, ratifying single-particle cryo-EM as an ideal choice for the structural elucidations. In the X-ray diffraction studies of abundant complexes such as ribosome and RNA polymerase II (pol II), cryo-EM data played instrumental roles for providing phase information (Ban et al., 1998; Fu et al., 1999). Henceforth, the growing demand on single-particle cryo-EM is anticipated.

Visualizing and analyzing single particles with molecular weight less than megadalton from cryo-EM images is faced with challenges for various causes (Frank, 2006), including low protein-to-solvent contrast, limited electron exposure, and moderate microscope signal transfer. Cryo-EM images of proteins are very noisy due to low electron exposure as proteins are radiation sensitive (Taylor and Glaeser, 1974). One important goal of single-particle cryo-EM is to achieve 4 Å, which allows identifying the secondary structures of proteins. Based on the experience with protein electron crystallography, it is estimated that millions of particles would be required for building up signals from the noises (Glaeser, 1999). In conventional EM (CEM), the contrast is further reduced by the suppression of low-resolution signals (Danev and Nagayama, 2001). For contrast recovery, large defocusing is necessary (Erickson and Klug, 1971). Defocusing, in combination with the spherical aberration of an objective lens, produces a contrast transfer function (CTF) (Thon, 1966) that band filters information in various resolutions. Determining CTF (Mallick et al., 2005; Sander et al., 2003; Zhou et al., 1996) and merging the CTF-corrected data from micrographs of various defoci are key steps to obtain high-resolution structures (Henderson et al., 1990).

A frequently asked question regarding cryo-EM is if it would be possible to be free of defocusing? The solution may lie in the use of a phase plate (Zernike, 1955), of which implementation to an EM had remained unsuccessful until a recent breakthrough by Nagayama (Danev and Nagayama, 2001), which rekindled a zealous pursuit for phase plate EM (Cambie et al., 2007; Shiue et al., 2009; Huang et al., 2006; Majorovits et al., 2007; Schultheiß et al., 2006). EM phase plate (Figure 1A), like its relative in a light microscope, is a quarter-wave plate that converts

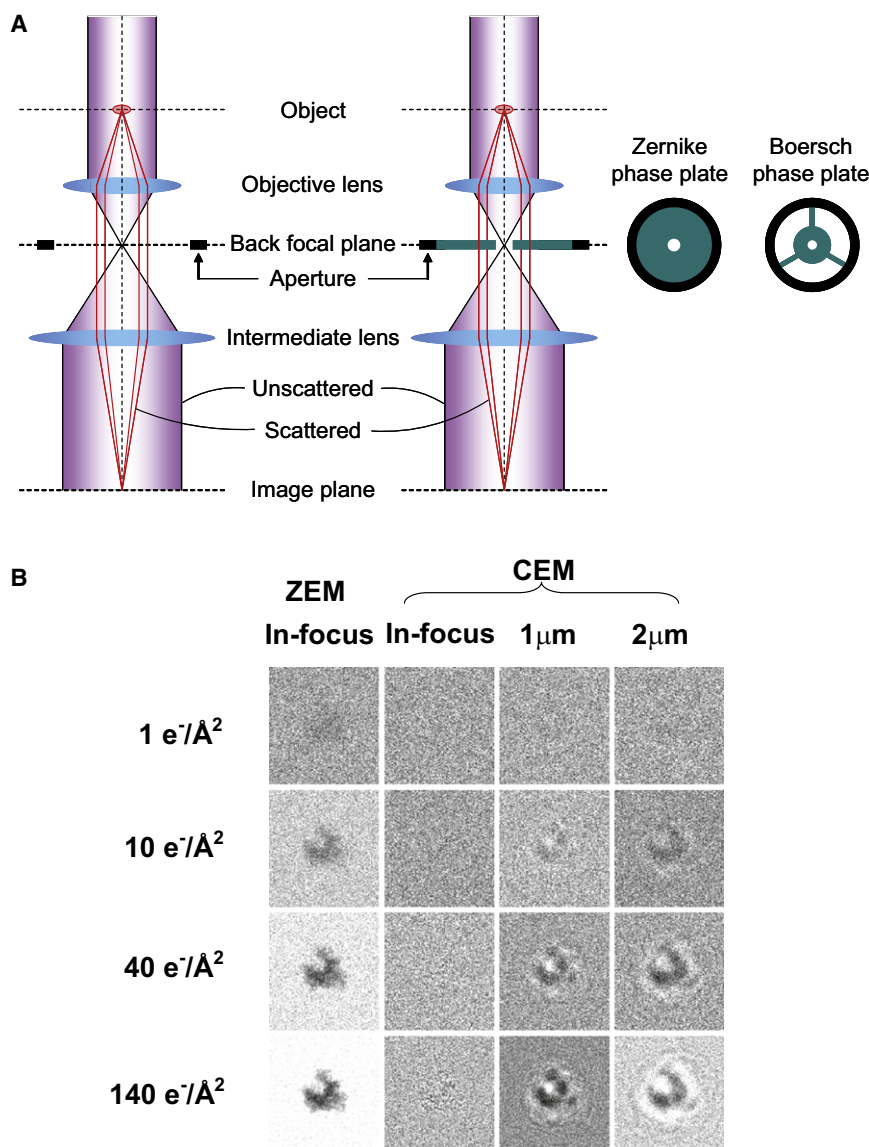


**Figure 1. Electron Microscopes and Simulated Electron Microscope Images of RNA Pol II**

(A) CEM on the left and ZEM on the right, made with insertion of a quarter wave plate in the back focal plane of the objective lens.

(B) Simulated pol II images from left to right are in-focus ZEM and defocused CEM 0.06, 1, and 2  $\mu\text{m}$ , respectively and from top to bottom are 1  $\text{e}^-/\text{\AA}^2$ , 10  $\text{e}^-/\text{\AA}^2$ , 40  $\text{e}^-/\text{\AA}^2$ , 140  $\text{e}^-/\text{\AA}^2$ , respectively.

plate? How much reduction of the required images for three-dimensional reconstruction at the subnanometer scale could be realized (Glaeser, 1999)? Also, how much reduction of molecular weight feasible with single-particle cryo-EM can be achieved with improved contrast by a phase plate (Henderson, 1995)? Here, to address these issues, we gauge the steps involved in single-particle analysis of images of protein complexes of low or no symmetry, obtained by in-focus ZEM or by large-defocused CEM, and compare the two techniques. Molecules between 100 and 500 kDa are recognized as the border zone of feasibility for single-particle cryo-CEM (Frank, 2006). We thus chose globular proteins of pol II (500 kDa), transferrin receptor complex (TfR; 290 kDa), and T7 RNA polymerase-lysozyme complex (T7 pol-lys; 100 kDa) as model molecules. Among various phase plates, we focused on “Zernike” for it gives non-astigmatic images (Majorovits et al., 2007), readily to be rotated in single-particle analysis. In order to study very large numbers of particle images with defined orientations and complexities, we resorted to simu-

lated cryo-EM images carrying characteristics comparable to experimental cryo-EM images.

the CTF of a sine type to a cosine type, restoring the phase contrast to a maximum level by an all-passing contrast transfer to  $\sim 4$   $\text{\AA}$  when operating in focus (Danev and Nagayama, 2001). To date, theoretical (Malac et al., 2007) and experimental works (Danev and Nagayama, 2008) on the applications of Zernike phase plate to imaging radiation-sensitive materials have been done. The former showed that Zernike phase plate was useful for reduction of electron doses, while the latter presented the first application of phase plate to single-particle cryo-EM and the authors showed that fewer particle images of GroEl (840 kDa), a protein-folding chaperon used as a cryo-CEM benchmark molecule (Ludtke et al., 2004; Stagg et al., 2006), were required to achieve a nanometer reconstruction than for CEM.

Still, quantitative aspects of what would be gained with a phase plate compared to the alternative large-defocused CEM as to single-particle analysis remain unclear. For instance, to what magnitude would the sorting of particle orientations and conformations benefit from the improved contrast by a phase

lated cryo-EM images carrying characteristics comparable to experimental cryo-EM images.

## RESULTS

### Contrast of the Simulated Images

Image contrast values were extracted from simulated images (Table 1). Image signal-to-noise ratio (SNR) is related to contrast C by the following equation:

$$\text{SNR} \approx C \times \sqrt{\text{dose}} \times d, \quad (1)$$

where  $d$  is the resolution, or the size of a pixel. Thus, SNR is resolution dependent and measures image contrast together with noise. It was found that (Table 1) a Zernike phase plate with a cut-on frequency of  $0.083 \text{ nm}^{-1}$  and 30% loss could restore  $\sim 75\%$  of the maximum contrast, provided by an ideal electron microscope, and lead to an  $\sim 3$ - to 4-fold gain of the image contrast or SNR over that obtained by a CEM with defocusing

**Table 1. Contrast of Simulated cryo-EM Images**

	Diameter (nm)	Ideal (lossless)	ZEM (lossless)	ZEM (30% loss)	Defocus ( $\mu\text{m}$ ) (CEM)					
					0.25	0.5	1	2	3	5
GroEI (840 kDa)	14	0.130	0.123	0.110	0.010	0.013	0.018	0.029	0.031	0.045
pol II (500 kDa)	13	0.125	0.111	0.095	0.017	0.022	0.026	0.033	0.036	0.038
TfR (290 kDa)	10	0.112	0.098	0.082	0.016	0.020	0.024	0.029	0.033	0.036
T7 pol-lys (100 kDa)	8	0.094	0.078	0.065	0.013	0.017	0.017	0.029	0.030	0.030

Cut-on frequency for ideal EM is  $0\text{ nm}^{-1}$  and for ZEM is  $0.083\text{ nm}^{-1}$ . GroEI was simulated by 300 kV (for ZEM with loss: 20%); others by 200 kV (for ZEM with loss: 30%). See also Table S1.

of 1–2  $\mu\text{m}$ , usually used for single particle cryo-EM imaging (Table 1). The cut-on frequency dependence of contrast for ZEM was studied and summarized (see Table S1 available online). When an ideal electron microscope was considered, the contrast of simulated pol II images was found to be 0.125 (Table 1), agreeing with 0.124, the value predicted by a combination of weak phase object approximation, a phase shift of 33 mRad per nm protein for 200 kV electrons (Wang et al., 2006), and treatment of pol II as a sphere of 10.5 nm diameter (see the calculations in the Supplemental Information). Similar results could be derived from the parameters provided by Rez (2003) by converting the phase shift from 100 kV to 200 kV. Such remarkable numerical consistency confirmed our simulation scheme was accurate and the usage of physical terms including material density and atomic scattering factor, but excluding CTF and noise, was appropriate.

### Comparison with Experimental Images

When a real electron microscope was considered, it is crucial to compare experimental data with the simulated images generated with the inclusion of CTF and noise. Image contrast (Danev and Nagayama, 2008) and image SNR (Malac et al., 2007) extracted from simulated CEM images were compared with those of experimental cryo-EM data. To suffice such, we collected a total of  $\sim 19,000$  cryo-CEM pol II images with  $10\text{ e}^{-}/\text{\AA}^2$  and 2  $\mu\text{m}$  defocus with small defocus spread (Figure 2A); SNRs measured from experimental cryo-CEM pol II images (2.25  $\text{\AA}$ ) had a distribution centering at  $\sim 0.23$  (Figure 2B), virtually identical with 0.234, the one obtained purely from simulation (use the contrast from Table 1 for 2  $\mu\text{m}$  together with  $10\text{ e}^{-}/\text{\AA}^2$  and 2.25  $\text{\AA}$  to plug in Equation 1), indicating that the simulated images were also good when CTF and noise were included. In addition, image alignment was performed on a limited number of experimental images and the attainable resolutions were compared to those from a similar number of simulated images. Cryo-CEM pol II data (2  $\mu\text{m}$  and  $10\text{ e}^{-}/\text{\AA}^2$ ) were first sorted according to the projections from an X-ray model (PDB 1WCM), namely by the supervised method (described in Experimental Procedures). A non-random distribution of orientations was found (data not shown): three abundant views insensitive to pol II clamp motion were selected. These classes contained 650, 871, and 1074 images, respectively. The images in each class were aligned and averaged and the resolution was assessed using Fourier ring correlation (FRC) to compare the averages from the half set in each class. The  $B_{\text{img}}$  of experimental data ( $\sim 2\text{ }\mu\text{m}$ ) was found to be  $\sim 90\text{ }\text{\AA}^2$  ( $\beta$ :  $\sim 0.13$  mRad). For rigorous comparison, the  $B_{\text{img}}$  factor used to model the simulated CEM images was also set to  $90\text{ }\text{\AA}^2$  ( $\beta$ : 0.13 mRad). The attainable resolutions and  $B_{\text{comp}}$  extracted from the

experimental data were found to be comparable with those from similar numbers of simulated images (Figures 2C and 2D). The factors of  $B_{\text{comp}}$  extracted from a limited number of images, experimental or simulated, were observed to gradually decrease to reach an asymptote, as more images were included for the alignment and averaging. We were thus concerned that estimating the number of particles required for a target resolution by extrapolating from the B factor derived from a limited number of images could be inaccurate and thus motivated to directly measure the relationship between the attainable resolution and the number of images by using large number of simulated images. As to ZEM, since we had no access to a ZEM, we compared the experimental ZEM GroEI images obtained in Nagayama's laboratory (Danev and Nagayama, 2008) with our simulated ZEM images. Simulated ZEM GroEI (data not shown) according to Nagayama's conditions (300 kV,  $25\text{ e}^{-}/\text{\AA}^2$ , 20% loss) gave a contrast value of 11% (Table 1), which is close to 10.4%, the one extracted from the experimental ZEM data (Danev and Nagayama, 2008). Simulated CEM GroEI images (300 kV,  $25\text{ e}^{-}/\text{\AA}^2$ , 2.5- $\mu\text{m}$  defocusing) gave a contrast of 3% (Table 1), close to 2.6%, the one extracted from the experimental CEM data by Danev and Nagayama (2008). In summary, the comparison of simulated images with experimental data indicated that the simulated images were good mimics of the experimental data to suffice the subsequent quantitative analysis.

### Single Particle Analysis of Simulated Images

#### Particle Selection

Automatic particle selection is a key for improving the throughput in single particle analysis (Glaeser, 2004). Two algorithms, EMAN and Agida's program (Adiga et al., 2004), were used to test how particle selection depended on SNR. Efficiency of selecting particles from images generated by in-focus ZEM and defocused CEM was compared for pol II, TfR, and T7 pol-lys (Figures 3A and 3B). As SNR is enhanced, the rates of false selection decrease while those of correct selection increase, independent of the algorithms. Among all, ZEM images, containing highest SNRs, allow for faithful selection. For CEM images, the larger the defocus is, the higher the correct rates are. A threshold of SNR of 0.3 at 2.25  $\text{\AA}$  pixel size was found, above which false rates diminished. For molecules smaller than 500 kDa, ZEM is capable of overcoming this critical SNR.

#### Classification

We compared the performance of sorting in-focus ZEM images with that of sorting defocused CEM images. The issue of heterogeneity in terms of orientation, conformation, and composition was treated one at a time.



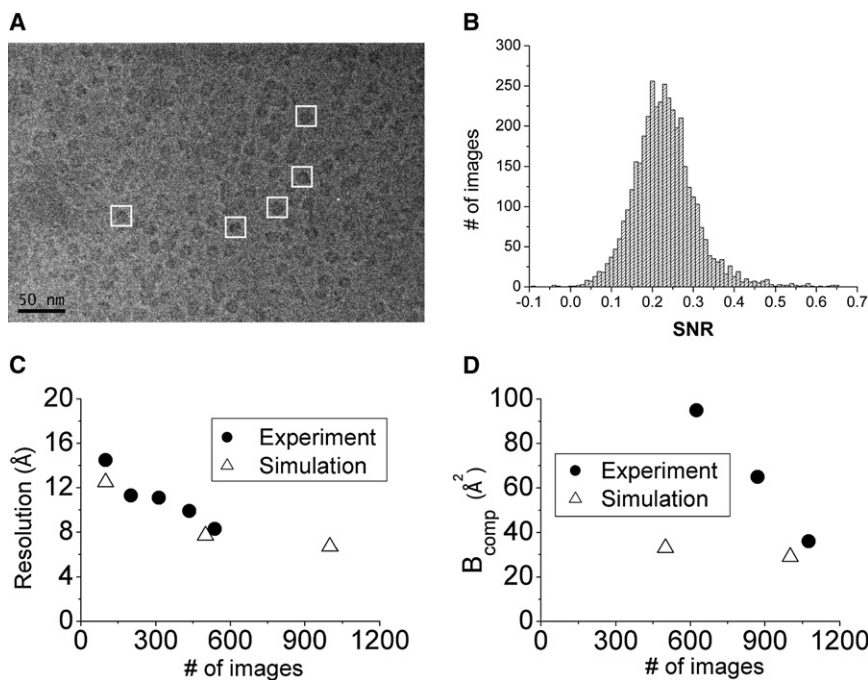


**Figure 2. Experimental Cryo-CEM of Pol II Data**

(A) A typical CCD image of pol II embedded in vitreous ice, imaged by a 200 kV cryo-CEM (defocus  $\sim 2 \mu\text{m}$ ,  $10\text{e}^-/\text{\AA}^2$ , 80,000 $\times$ ).

(B) A histogram of image SNRs measured from thousands of pol II images.

(C) Attainable resolutions from a limited number of pol II images versus those from simulated images.

(D) Extracted  $B_{comp}$  from experimental pol II images versus those from simulated images.

### Orientation

A mixture of 20 views of pol II in a single conformation (1K83) was studied. Nine clusters corresponding to nine views were randomly selected for displaying on a factor map (Figure 4A). Clusters of simulated 0.5  $\mu\text{m}$ -defocused CEM images overlap seriously, as expected for low-contrasted images. As contrast was increased by using large-defocused CEM or in-focus ZEM, clusters gradually separated. Both 2  $\mu\text{m}$ -defocused CEM and ZEM rendered nearly all nine views dispersed on the factor maps. Percentages of resolvable clusters were summarized (Table S2), indicating the best result is given by ZEM. Notably, orientations of T7 pol-lys could no longer be separated, indicating 100 kDa is about the size limit for resolving different views.

### Conformation

Pol II was chosen as a model to address this issue as conformational flexibility is a feature shared by many RNA polymerases (Area et al., 2004; Darst et al., 2002; De Carlo et al., 2003). Such feature underlies the difficulty in resolving pol II structure beyond subnanometer by single particle analysis (Kostek et al., 2006). To study the effect of contrast on sorting conformations, a mixture of two pol II conformations, corresponding to the open Rpb1 clamp and the closed, was used. The swinging movement of the clamp from the open to the closed conformation measures to about  $22.5^\circ$  (Figure S2A). The sorting of the mixed conformation is shown in Figure 4B. Notably, ZEM separates the two conformers into two clusters, while CEM does not. Whether ZEM could resolve finer clamp motion was tested by studying a mixture of three clamp conformers spaced by  $\sim 10^\circ$ , from the open toward the closed. As the conformational difference was set to this magnitude, the distribution of clusters evolved from being “disjoint” to “continuous” so that the conformers were hard to be separable even with ZEM (Figure S3).

### Composition

Compositional heterogeneity in protein complex presents an additional complexity: an isolated protein complex may not contain all subunits. For example, yeast pol II usually comprises two populations as its Rpb4-Rpb7 subunit is underexpressed or dissociable (Edwards et al., 1991). ZEM was compared with CEM in disentangling images containing mixture of 10 subunit (lacking Rpb4-Rpb7) and 12 subunit pol

II (Figure S2B). ZEM as well as CEM with sufficient defocus (0.5–2  $\mu\text{m}$ ) could resolve the mixture into two distinct clusters (Figure 4C). The resolvability of pol II composition was found to be view independent, as the sorting at an orthogonal view, where Rpb4-Rpb7 was obscured, gave the same result (data not shown). Nevertheless, pol II failed to be resolved from pol II/TFIIB finger (Bushnell et al., 2004) by CEM or ZEM (data not shown), suggesting that the separation of compositions depends on the size of the varying piece.

### Alignment/Averaging and Resolution Regular Electron Microscope

Regular EM was modeled with a defocus-dependent spatial coherence ( $\beta$ : 0.2 mRad). The relationship between resolutions and the number of projections was measured for various imaging conditions (Figure S4; Figure 5). The number of particles reaching milestone resolutions was tabulated (Table 2). For defocused CEM, such a relationship was found to be sensitive to defocus, unnoticed previously. We noticed that  $\sim 100$  CEM pol II projections (0.5–2  $\mu\text{m}$ ) could reach nanometer resolution (11  $\text{\AA}$ ), whereas  $\sim 50$  ZEM (in-focus) pol II projections were sufficient. Such a 50% reduction of images for a molecule as large as pol II (500 kDa) by ZEM to reach nanometer is parallel to a similar figure (30%) observed for GroEl (840 kDa) to a similar resolution (Danev and Nagayama, 2008). To reach 4.5  $\text{\AA}$ , a resolution at which protein secondary elements can be visualized (Ludtke et al., 2008),  $\sim 40,000$ – $200,000$  CEM images of pol II (0.5–2  $\mu\text{m}$  defocus) were required (Figure 5A and Table 2), consistent with what was observed for GroEl to reach the same resolution (Ludtke et al., 2008). So far, there is yet to be a ZEM experiment performed to reach 4.5  $\text{\AA}$ . By using simulated images, we predict that  $\sim 15,000$  ZEM images of a molecule of the size of pol II are sufficient to reach this resolution, which is readily testable by the experiments. To reach near atomic resolution (3.3  $\text{\AA}$ ), the

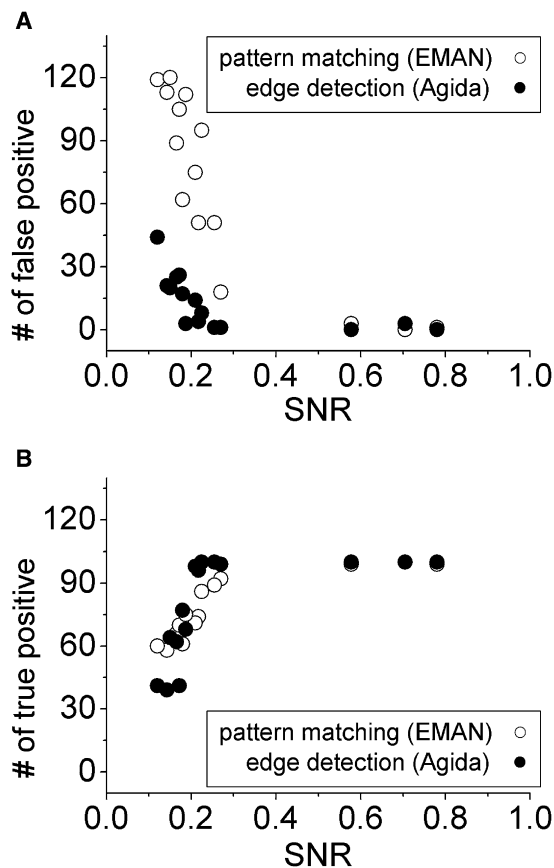


**Figure 3. Frequency of Automatic Particle Selection Versus Image SNR**

(A) False positive frequencies were measured by selecting from 100 simulated images of pol II, Tfr, and T7 pol-lys under contrast conditions by in-focus ZEM and CEM of 0.5, 1, and 2  $\mu\text{m}$ , indexed by the respective SNRs ( $10\text{e}^{-}/\text{\AA}^2$ , 2.25  $\text{\AA}$ ).

(B) Correct selection frequency. See also Figure S1.

difference in the required data between CEM and ZEM for pol II was found to be  $\sim 10$ -fold (Figure 5A and Table 2).

Aligning cryo-EM single particle images of proteins may find a limit near 100 kDa. Currently, spliceosomal particle U1 of 200 kDa, aided by the signals arising from its RNA component, is the smallest molecule analyzed with cryo-EM (Stark et al., 2001). To investigate if ZEM would impact aligning images of smaller proteins, Tfr (290 kDa) and T7 pol-lys (100 kDa) were studied. Our results showed that ZEM also reduced the number of particles required for Tfr and T7 pol-lys (Figures 5B and 5C and Table 2). As the resolution was extended into subnanometer resolution, more images were required. Interestingly, for ZEM to reach 4.5  $\text{\AA}$  (Table 2), 16,000 Tfr and 62,000 T7 pol-lys were required, respectively, while for CEM, 600,000 Tfr (1  $\mu\text{m}$ ) and more than one millions of T7 pol-lys (1  $\mu\text{m}$ ) were required, respectively, suggesting ZEM would be more efficient for studying small proteins to subnanometer resolution.

#### Coherent Electron Microscope

Interestingly, the best result of image alignment for a regular CEM does not arise from the highest defocus (Figure 5). Such

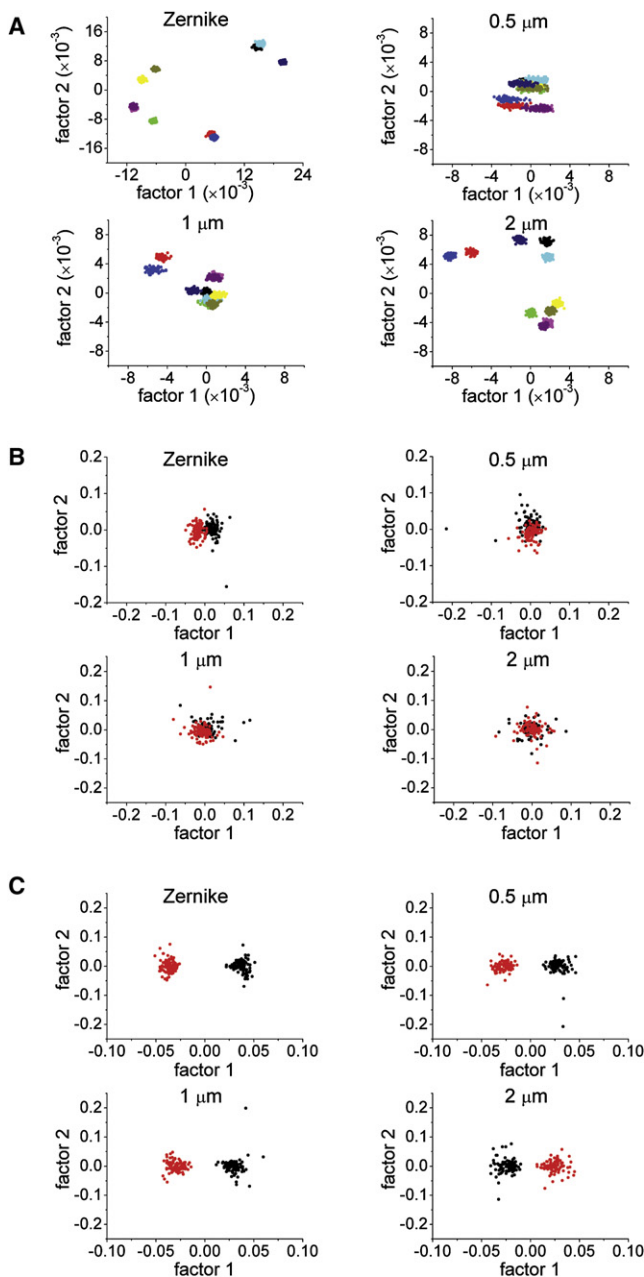


**Figure 4. Factor Maps from Classification**

(A) Clusters representing nine orientations of pol II, obtained by in-focus ZEM and CEM with 0.5, 1, and 2  $\mu\text{m}$ , respectively.

(B) Clusters representing two pol II conformations: 1K83(clamp 67°) and 116H-DNA/RNA (45°) conditions as in (A).

(C) Clusters representing two pol II compositions: 1WCM and 1K83 conditions as in (A). See also Figures S2 and S3 and Table S2.

a finding, together with the finding that large defocus is crucial for image identification and classification, supports the rationale for a defocus pair strategy (Cheng et al., 1992; Ludtke and Chiu, 2003). We suspected that the less than optimal alignment of large-defocused images might arise from the fast decay of signals caused by the defocus-dependent spatial coherence (Equations 10 and 11). We were also concerned whether the

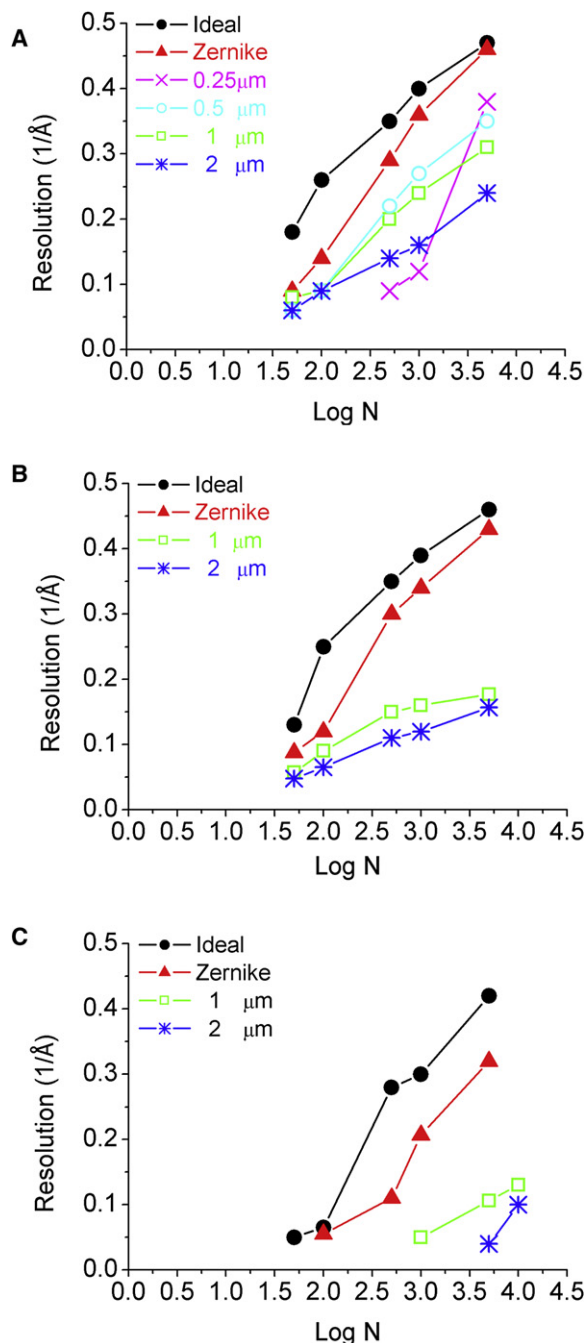


**Figure 5. Relationship between the Attainable Resolutions Versus Number of Aligned Images**

(A) pol II.

(B) TfR.

(C) T7 pol-lys [x axis: logarithm of the number of images; y axis: resolution ( $1/\text{\AA}$ )]. See also Figures S4 and S5 and Table 2.

reason ZEM worked better than regular CEM was because ZEM was less susceptible to the defocus-dependent spatial coherence as ZEM was operated in focus. We wondered how much better a coherent EM ( $\beta$ : 0 mRad) would perform than a regular CEM ( $\beta$ : 0.2 mRad). In principle, a coherent EM can be realized

by using an electron emitting from a very sharp field emission tip: we modeled coherent CEM by setting both spatial coherence and temporal coherence to unity. Interestingly, improved coherence only led to a minor improvement in image alignment for CEM. Regardless of the coherence, CEM images with 1  $\mu\text{m}$  defocusing were always better aligned than those with 2  $\mu\text{m}$ , (Figure S5), suggesting that the high-resolution signal, restored by coherence, does not play a significant role in image alignment. In contrast, ZEM, coherent or partially coherent, was superior to coherent CEM (Figure S5). By integrating the signals in the power spectra (Frank, 2006), we found that 1  $\mu\text{m}$  and 2  $\mu\text{m}$  coherent CEM transmitted a similar amount of spectral signals (Figure S6 and Figure 6), suggesting CTF may have played a profound role in aligning noisy images. Perhaps image delocalization induced by large defocus would cause deficit to alignment.

#### Ideal Electron Microscope

We wondered what would be the minimum amount of data required for 3D reconstruction by an ideal EM, which we modeled with a unity CTF and zero cut-on frequency. Realistically, an ideal EM can be realized by a combination of a lossless Zernike phase plate with reduction of the cut-on frequency and correction of the spherical aberration Cs (Haider et al., 2008). As shown in Table 2, ~13,000 pol II, ~21,000 TfR, and ~66,000 T7 pol-lys, all of a unique conformation, were the respective minimum numbers required by an ideal EM for reaching 3.3  $\text{\AA}$ .

#### DISCUSSION

In this work, we demonstrated that a Zernike phase plate with a cut-on frequency of  $0.083 \text{ nm}^{-1}$  and 30% loss could restore ~75% of the maximum phase contrast provided by an ideal electron microscope. Such contrast enhancement leads to an ~3- to 4-fold gain of the image SNR over that obtained by a CEM with defocusing of 1–2  $\mu\text{m}$  (Table 1), in good agreement with experimental observations (Danev and Nagayama, 2008). As such, “in silico” fractionation of the ZEM images of mixed views, or of mixed conformations, can be improved, reducing the likelihood of reconstructing a structure from unresolved orientations, or from multiple conformations or compositions. Henceforth, Zernike phase plate may bear critical importance to extending the resolution for the single-particle reconstruction technique, a method posing little constraint on orientations and molecular complexity (Scheres et al., 2007a, 2009). Separation of molecular complexity by ZEM could be instrumental to the study of assembling and disassembling of cellular machineries involved in transcription, splicing, and translation that usually comprise abundant conformational and compositional dynamics.

The notion that image contrast is crucial for image alignment (Rosenthal and Henderson, 2003) implies that improved contrast by ZEM could relax the resolution limits imposed by imperfect alignment of single particle images (Jensen, 2001). By measuring the attainable resolution with a given number of images, we demonstrated that ZEM indeed improved image alignment. Interestingly, the observation that aligning the CEM images is sensitive to defocus suggests that CTF may play a profound role in alignment and that the cause of ZEM images championing in alignment is most likely due to the all-pass CTF of ZEM. As

**Table 2. Total Number of Particles Required to Reach a Target Resolution**

	Resolution (Å)	Ideal	ZEM (30% loss)	Defocus (μm) (CEM)			
				0.25	0.5	1	2
pol II	11	~800	~1,570	NA	~3,200	~2,200	~3,200
	4.5	~4,800	~15,000	<500,000	~38,000	~48,000	~240,000
	3.3	~13,000	~60,000	<500,000	~260,000	~400,000	>500,000
TfR	11	~800	~1,400	NA	NA	~3,900	~6,400
	4.5	~5,000	~16,000	NA	NA	>600,000	>600,000
	3.3	~21,000	~48,000	NA	NA	>1,000,000	>1,000,000
T7 pol-lys	11	~4,000	~6,400	NA	NA	~63,000	~160,000
	4.5	~21,000	~62,000	NA	NA	>1,000,000	>1,000,000
	3.3	~66,000	~160,000	NA	NA	>1,000,000	>1,000,000

near-atomic resolution is aimed, ZEM helps reduce the total number of particles required for 3D reconstruction. The factor of reduction, defined by the number required by an optimal defocused CEM over that by a ZEM, depends on the size of the molecule. For example, in the case of a 30S ribosome (data not shown), the factor is close to one. As the size of the molecule decreases from that of pol II (500 kDa) to T7 pol-lys (100 kDa), the factor gradually increases from 10 to 100. When a protein as small as bacteriorhodopsin (~30 kDa) was studied, neither the CEM nor ZEM images could be aligned (data not shown), suggesting a cut-off in molecular weight defining the feasibility of cryo-EM existing between 30 and 100 kDa (Henderson, 1995). When an ideal EM was applied to a molecule of single conformation with the size of pol II, the minimum number required for 3D reconstruction was found to be ~10,000, echoing a previous theoretic estimate (Henderson, 1995), also in the absence of CTF. Currently, to reach atomic resolution by a conventional cryo-EM, ~1,000,000 asymmetric units are required (Chen et al., 2009a). This study thus suggests that Zernike phase plate may help narrow the gap. It is hoped this very feature of Zernike phase plate may aid the structural proteomics of scarce protein complexes.

In summary, we conclude that Zernike phase plate EM facilitates single particle cryo-EM with various aspects discussed above. It is perceived that electron tomography, where signals are compromised by fractionated dose, large defocusing, and thick ice, may also benefit from a Zernike phase plate. Finally, the simulation scheme in this study may present as a useful tool for the cryo-EM community when analytical or experimental approach is out of reach. It is interesting to examine if the quantities derived in this study would remain robust under a more realistic noise model (Scheres et al., 2007b). The issue of optimizing the cut-on frequency with respect to the size of a protein (Danev et al., 2009) will be addressed fully in a separate paper.

## EXPERIMENTAL PROCEDURES

### Experimental Section and Data Analysis

#### Data Collection

Twelve subunit pol II with a TAP tag was purified from yeast as described (Chen et al., 2009b). A pol II aliquot [~1 mg/ml, in 200 mM KOAc, 50 mM Tris-HCl (pH 7.5), and 10% glycerol] was diluted 20 times with deionized water. Approximately 3 ml of protein solution were applied to an amyl-acetate-treated quantifoil grid, blotted, and flash-plunged into liquid ethane. Cryo-EM imaging was performed under low-dose conditions on a 200 kV electron microscope

(JEOL 2011; Cs: 1.0 mm, ~2 μm defocusing, ~10e<sup>-7</sup>Å<sup>2</sup>). Images were recorded with microscope magnification of 60,000× on Kodak SO films or on a CCD (Gatan 894: 18 μm, 2K × 1.5K, effective magnification: 80,000×). Micrographs were digitized with a Z/I flat-bed densitometer with a 14 μm step size. Pol II particles were selected and boxed using EMAN (Ludtke et al., 1999).

#### Extraction of Image Contrast and Contrast-to-Noise Ratio

Image contrast (C) was extracted from images according to the following equation:

$$C = (I_p - I_{ice}) / I_{ice}, \quad (2)$$

where  $I_p$  and  $I_{ice}$  are the average gray levels in the protein region and in the surrounding ice, respectively. Image SNR (Malac et al., 2007), or contrast-to-noise ratio (Chiu and Glaeser, 1975; Glaeser, 1999; Rose, 1948), is given by

$$SNR = (I_p - I_{ice}) / sd, \quad (3)$$

where  $sd$  stands for the standard deviation of gray levels in the surrounding ice. Pixels containing Fresnel fringes on the protein-ice boundary were excluded.

#### Image Classification, Alignment/Averaging, and Resolution

Experimental cryo-CEM pol II images were sorted with supervised classification (Craighead et al., 2002; Gao et al., 2004): each image was assigned to a view class based on the highest cross-correlation score with a gallery of 83 views of 2 μm-defocused pol II (1WCM) potential map. Three abundant classes, insensitive to the Rpb1 clamp motion, were selected for reference-free alignment on the SPIDER suite (Frank et al., 1996). Two averages generated from odd and even number images in each class were compared for resolution assessment using an FRC coefficient of 0.5.

#### B Factor Analysis

B factor-dependent envelope is useful to delineate signal decay versus resolution due to compounded image degradation effect

$$E = \text{Exp}(-B\kappa^2) \quad (4)$$

(Jensen, 2001). By excluding MTF, the Fourier transform of an EM image can be approximated by the following equation:

$$F\{I\} \approx [SF(\kappa) + b] \times CTF \times \text{Exp}(-B_{img}\kappa^2) + n, \quad (5)$$

where  $F\{\}$  denotes forward Fourier transform,  $SF$  the structure factor,  $\kappa$  spatial frequency,  $b$  background, and  $n$  shot noise. From an entire CCD image or a micrograph, average power spectra were calculated by adding spectra of subareas to extract  $B_{img}$  according to

$$P_{avg}(\kappa) = \sum \|F\{I\}\|^2 \approx (\|SF(\kappa) + b\|_{avg})^2 \times CTF^2 \times \text{Exp}(-2B_{img}\kappa^2). \quad (6)$$

As many particle images of the same view and defocus were aligned and averaged, an average structure factor of the molecule is given by the following equation:

$$SF_{avg}(\kappa) \approx SF_{mol} \times CTF \times \text{Exp}(-B_{total}\kappa^2). \quad (7)$$



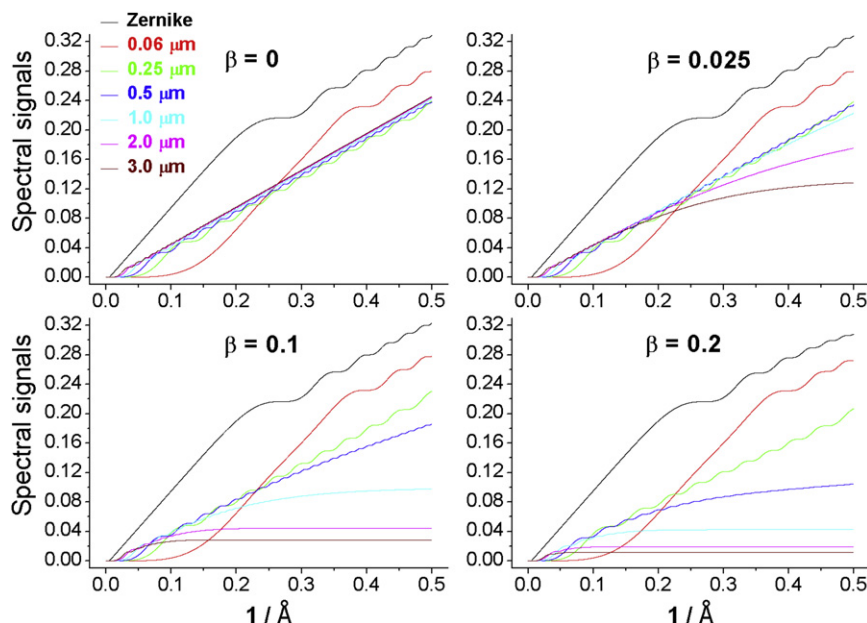


**Figure 6. Spectral Signals Versus Resolution**

Spectral signals were obtained by performing integration of the square of CTF to a resolution; CTF modulated by various spatial coherence envelope functions.  $\beta$  represents the electron source divergence, varying from 0 to 0.2 (mRad). Zernike represents in-focus ZEM (lossless). The defociuses used for CEM are as follows: 0.06, 0.25, 0.5, 1, 2, 3 ( $\mu\text{m}$ ). See also Figure S6.

### Ice Embedding

The embedding scheme is depicted in Figure 7A. 1.3 g/ml and 0.94 g/ml were adopted for the density of protein and that of amorphous ice, respectively. Ice thickness was assumed to be 300 Å. First, the PDB of a molecule (pol II:1K83, 1WCM, 1I6H; Tfr: 1SUU; T7 pol-lys: 1AR0) was placed in vacuum and converted to a SPIDER volume by “CP from PDB” with a pixel of 1 Å to generate 83 15°-spaced projections by “PJ 3Q” (Frank et al., 1996). The projections were converted to TIFF format (8-bit) by “CP to TIFF” and the subsequent formation of electron microscope images were performed with Matlab. The local thickness of the molecule,  $t_p(x, y)$  Å, was obtained:

$$t_p(i, j) = t_{\max} \times I(i, j) / I_{\max}, \quad (11)$$

where  $I_{\max}$  was the darkest level in the projection,  $I(i, j)$  the gray level at pixel  $(i, j)$ , and  $t_{\max}$  the longest thickness of the volume viewed from the side, perpendicular to the projecting direction (for pol II,  $t_{\max}$  is between 12 and 15 nm). Second, the molecule was placed in an ice layer: the local ice thickness at pixel  $(i, j)$  was assigned to be  $[300 - t_p(i, j)]$  Å. The total number of various atoms in the column of  $t_p$  (protein) plus  $(300 - t_p(i, j))$  (ice) was calculated according to:

$$N_x = f_x^p \times t_p \times 1.3/6.68 + f_x^{ice} \times (300 - t_p) \times 0.94/6 \times N_A/10^{24}, \quad (12)$$

where  $N_x$  is the number of atoms of type  $x$ ,  $f_x^p$  the fraction of the atom in protein, and  $f_x^{ice}$  that in ice;  $N_A$  Avogadro number; 6.68 (Dalton) the average atomic mass in protein and 6 the one in ice. For instance, the number of carbon (comprising ~31% of a protein) was given by

$$N_c = (0.31 \times t_p \times 1.3/6.68) \times N_A/10^{24}, \quad (13)$$

and the number of oxygen (comprising ~8% of a protein) was given by

$$N_o = (0.08 \times t_p \times 1.3/6.68 + 0.33 \times (t - t_p) \times 0.94/6) \times N_A/10^{24}. \quad (14)$$

The number of hydrogen atoms (52.5% of a protein and 66.6% in ice), nitrogen (8% in protein), and sulfur (5% in protein) were calculated accordingly.

### Calculating Projected Potential Map, Exit Wave, and Electron Microscope Images

Apart from ice embedding, the following modeling is virtually identical to a published protocol (Sugitani and Nagayama, 2002). Atomic scattering factors,  $f_s$ , were taken from the table values in Fultz and Howe (2005). The projected potential  $V(i, j)$  of a molecule was calculated according to the following equation:

$$V(x, y) = \int V(x, y, z) dz = F^{-1} \left\{ \left[ \sum_x F[N_x(x, y)] \times f^x(\kappa) \right] \right\} / \sigma, \quad (15)$$

where  $\sigma$  is  $\lambda m_e e^2 / h^2$ , the interaction constant.  $V$  comprises real and imaginary parts, and so does the atomic scattering factor

$$V(x, y) = V_r(x, y) + i V_i(x, y); \quad V_i \sim 0.1 V_r. \quad (16)$$

The exit wave thus reads as

$$\Psi_{ex}(x, y) = \Psi_{in}(x, y) \times \text{Exp}\{i\sigma \times t \times V(x, y)\}. \quad (17)$$

By Equation 7,  $B_{\text{total}}$  was extracted with Guinier analysis by plotting  $\ln(SF_{\text{avg}}/SF_{\text{mol}})$  against  $\kappa^2$  in  $[0, 0.01] \text{ \AA}^{-2}$  (Rosenthal and Henderson, 2003).  $SF_{\text{mol}}$  was calculated based on atomic scattering factors and PDB coordinates.  $B_{\text{total}}$  was decomposed into:

$$B_{\text{total}} = B_{\text{img}} + B_{\text{comp}} \quad (8)$$

(Rosenthal and Henderson, 2003). Like FRC,  $B_{\text{comp}}$  also reports the performance of image alignment.

### Simulation Section and Single Particle Analysis

#### Imaging Parameters

Images of pol II, Tfr, and T7 pol-lys were simulated (200 kV, Cs: 1.0 mm,  $\lambda$ : 0.0251 Å,  $10e^-/\text{\AA}^2$ ) according to

$$I(x, y) = \|\Psi_{ex}(x, y) \otimes F^{-1}[E_s(\kappa)E_t(\kappa)A(\kappa)\exp(i\gamma(\kappa))]\|^2 + \text{noise}, \quad (9)$$

where  $F^{-1}\{\}$  denotes backward Fourier transform;  $\otimes$  convolution,  $E_t(\kappa)$  partial temporal coherence envelope function  $\exp[-(\pi \lambda \delta Z \kappa^2 / 2)^2]$ ;  $E_s(\kappa)$  partial spatial coherence envelope  $\exp[-\pi^2 q^2 (\lambda \Delta Z \kappa - \lambda^3 C_s \kappa^3)^2]$ ;  $A(\kappa)$  aperture function;  $\exp(i\gamma(\kappa))$  complex CTF;  $q$  effective source size ( $\text{\AA}^{-1}$ ); and  $\beta$  effective source divergence (Rad) ( $\beta = q \times \lambda$ ). For CEM, defociuses in the range from 0.06 to 5  $\mu\text{m}$  were used. For ZEM, in focus was used by setting the  $\Delta Z$  in  $E_s(\kappa)$  to be zero; cut-on frequency of 0.083  $\text{nm}^{-1}$  was chosen by taking 1 pixel from 128 pixels spanning  $[0, 1] \text{ \AA}^{-1}$ . 0.083  $\text{nm}^{-1}$  corresponds to a hole of 1.2  $\mu\text{m}$  diameter when a focal length of 3 mm is considered, proximal to the parameter used by Nagayama (Danev and Nagayama, 2001; Danev et al., 2009) and it is suitable for pol II, Tfr, and T7 pol-lys. 300 kV microscope images of GroEl were also simulated (Cs: 3.7 mm,  $\lambda$ : 0.0196 Å,  $25e^-/\text{\AA}^2$ ; in-focus for ZEM and 2.5  $\mu\text{m}$  defocus for CEM). Throughout this study,  $E_t$ , the temporal coherence function, was assumed to be unity.  $E_s$ , the partial spatial coherence, was modeled with a source divergence of 0 (coherent) or 0.2 mRad (partially coherent) to give a defocus-dependent envelope of

$$E_s(\kappa) = \exp \left[ -\pi^2 q^2 (\lambda \Delta Z \kappa - \lambda^3 C_s \kappa^3)^2 \right]. \quad (10)$$

The amplitude contrast was set to be 10% (Frank, 2006). The phase shift by Zernike phase plate was set to be 90° and a variation of 5° was used to depict the plate roughness. The plate transmittance for 200 kV electrons was assumed to be 70%, namely 30% loss (Danev and Nagayama, 2001), while “lossless” stood for 100% transmittance.



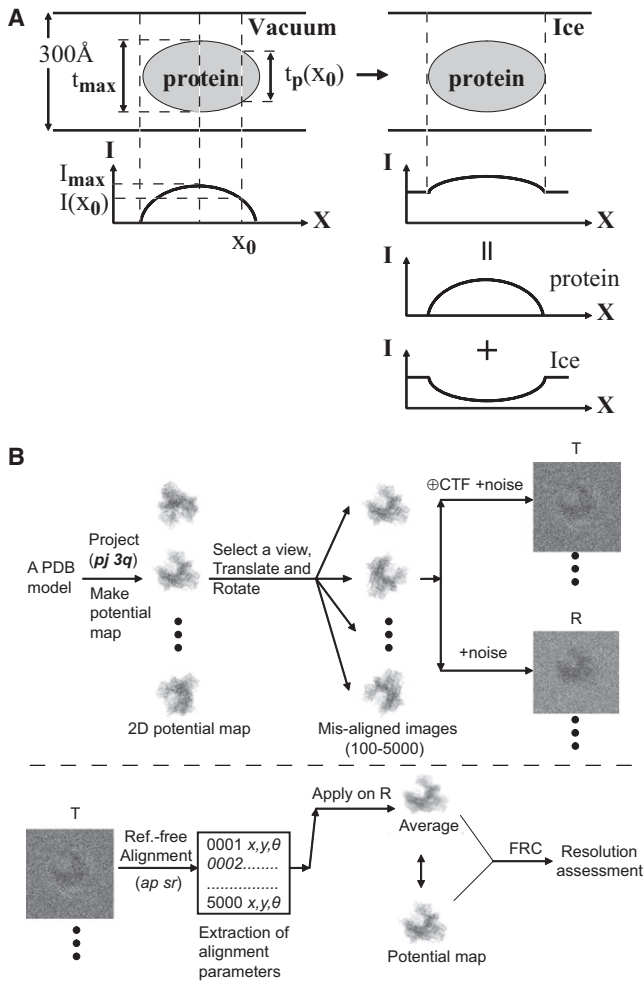


**Figure 7. Embedding Protein in Ice and Making Simulated Electron Microscope Images**

(A) A protein was immersed in vacuum to generate a potential map. Vitreous ice of 30 nm was filled into the protein-void region to generate an ice potential map. The two maps were summed.

(B) Generation of simulated EM images with randomized translation and rotation (top). T contains EM images and R is identical to T except without CTF and envelope functions. (bottom) Alignment parameters were extracted from T but applied to R to generate averages, compared with the noise-less potential maps by FRC for resolution assessment.

The wave function and the resultant image at the image plane read as

$$\Psi_{img}(x, y) = \Psi_{ex}(x, y) \otimes F^{-1}[E_s(\kappa)A(\kappa) \exp(i\gamma(\kappa))] \quad (18)$$

and

$$I_{img}(x, y) = \|\Psi_{img}(x, y)\|^2 + \text{noise}, \quad (19)$$

where  $E_s$  is the partial spatial coherence envelope,  $A$  the aperture function, and  $I_{img}$  the electron microscope image.  $\exp(i\gamma(\kappa)) = \cos\gamma(\kappa) + i\sin\gamma(\kappa)$  is the complex CTF function. Equation 18 can be rewritten as follows for the ease of computation:

$$\Psi_{img} = \Psi_{in} \times F^{-1} \left[ F \left( \exp \left\{ iF^{-1} \left[ \left( \lambda \times \sum_{\kappa} F[N_{Xp}] f^X(\kappa) \right) \right] \right\} \right) \right. \\ \left. \times E_s(\kappa)A(\kappa) \exp(i\gamma(\kappa)) \right]. \quad (20)$$

For ZEM, a phase shift of  $\alpha = \alpha_r + i\alpha_i$  was added to  $\gamma$ , where  $\alpha_i$  was used to model the loss through the plate.  $\alpha_i$  ( $\sim 0.1 \alpha_r$ ) was consistent with the 30% loss when  $\alpha_r$  is  $90^\circ$ . Shot noise was modeled by zero-mean Gaussian noise with variance equaling to the number of electrons per pixel: for example, a dose of  $10 \text{ e}^-/\text{\AA}^2$  gives noise intensity of  $\sqrt{10}$  in a pixel of  $1 \text{ \AA}$ . The dataflow is briefed in Figure 7B. In our simulation, full exit wave was used for numerical accuracy. It is useful to gain insight by weak phase approximation, under which the SNR of a CEM image reads as

$$\text{SNR}_c(x, y) \sim 2\sqrt{N_0} \times \lambda \times F^{-1} \left\{ \left( \sum_{Xp} F[N_{Xp}] f^{Xp}(\kappa) - \sum_{Xice} F[N_{Xice}] f^{Xice}(\kappa) \right) \right. \\ \left. \times E_s(\kappa) \sin\gamma(\kappa) \right\} \quad (21)$$

and that of an ZEM image reads as

$$\text{SNR}_z(x, y) \sim 2\chi\sqrt{N_0} \times \lambda \times F^{-1} \left\{ \left( \sum_{Xp} F[N_{Xp}] f^{Xp}(\kappa) - \sum_{Xice} F[N_{Xice}] f^{Xice}(\kappa) \right) \right. \\ \left. \times E_s(\kappa) \cos\gamma(\kappa) \right\}, \quad (22)$$

with  $\chi$  equal to 0.85 based on the 70% transmission through the plate. It is then evident that  $\text{SNR}_z$  is greater than  $\text{SNR}_c$ .

#### Preparing Simulated Images for Particle Selection, Classification, and Alignment

Single particle analysis commonly involves three major steps: particle selection, image classification, and image alignment. They are performed sequentially over the same data set. To eliminate the propagation of errors from one step to the next, we generated different sets of data as separate inputs for the three steps. We were able to decouple the performance of each step. For particle selection, 100 noisy replicas of a simulated image of a molecule in a single view/conformation (Figure 1B) were created, centered in a grid of 250 pixels. One hundred grids were tiled into a “big micrograph” (Figure S1). For image classification, three sets of simulated images containing mixed orientations, mixed conformations, and mixed compositions were created. To reduce error propagation arising from aligning noisy and CTF-degraded images prior to classification, potential maps of various orientations (conformations or compositions) were aligned before derivativizing their corresponding images. For mixture of orientations, 20 views were chosen from 83 views generated with  $15^\circ$  Euler angle spacing (PDB 1K83, 1SUU, and 1ARG). One hundred noisy replicas of the 20 views were generated and mixed to form a set of a total of 2,000 images. As for mixture of conformations, a union set was formed by including pol II images of clamp-open view (1K83) and the ones of closed view. First, the closed form, termed 116H-DNA/RNA, was generated from the elongation complex (116H) by removing the RNA and DNA; second, The SPIDR volume of 116H-DNA/RNA was aligned against that of 1K83 (SPIDER operation: OR 3Q) and 83 aligned view pairs were created; third, a view pair (Figure S2A) most sensitive to the clamp movement was chosen; fourth, 100 noisy replicas of the view pair were generated and mixed. A further study was done on the same view consisting of three conformers, created by modeling the movement of the Rpb1 clamp in 1WCM from the open position to the closed position with a step of  $10^\circ$ . As to the mixture of composition, simulated images of 12 subunit pol II (PDB 1K83, lacking Rpb4-Rpb7) in the same view were mixed. To do so, the volume of 1WCM, with the Rbp4-Rpb7 removed, was aligned to that of 1K83 by SPIDER operation (OR 3Q). The parameters of alignment were extracted and applied to 1WCM and 83 view pairs were made. A pair of views was selected (Figure S2B) and 100 replicas were generated and mixed. To make simulated images for alignment, a set of misaligned images of a molecule in a single view/conformation was created by randomly rotating and translating the potential map (maxima shift is  $20 \text{ \AA}$  and rotation in a full circle), followed by convoluting with CTF and envelope function, and addition of noise. Such set is termed “template set” T, from which a “replica set” R (Figure 7B) was made with identical misalignment and noise but without convoluting with CTF and envelope function. Hence, R was free of CTF and B factor. The number of images in a set of for alignment ranged from 50 to 5000.

## Single Particle Analysis of Simulated Images

## Particle Selection

Two methods for automatic particle selection were used: one was based on a template matching method, performed with EMAN; the other was based on an edge detection method, performed with Adiga's program (Adiga et al., 2004). On EMAN, ten training particles were manually selected, followed by the "auto-selection function." The output was a set of particle centroids. The distance between the center of the grid and the predicted centroid was calculated. "True positive" was decided if the distance was shorter than 25 Å, ~10% of the box size, whereas "false positive" was decided otherwise. If the predicted coordinates fell outside the grid, a miss-of-hit was counted.

## Classification

We used the unsupervised classification method (Fu et al., 2007) to sort the simulated images as it requires no priori knowledge of the molecule. To do so, correspondence analysis was used and the resultant clusters in the multidimensional factor space were tracked (Fu et al., 2007), without further partitioning by K means, hierarchical ascendant, or maximum likelihood (Scheres et al., 2007a). Correspondence analysis (CA) is a multivariate statistical analysis technique used in single particle analysis: an image of J pixels is represented with a vector of J dimension hyperspace; a set of vectors corresponding to noisy replicas of the image would form a cluster in the hyperspace; to analyze a mixture of N images, a matrix of J \* N and its co-variance matrix are computed (SPIDER operation of "CA S"), from which the eigenvectors, or factors, are determined (Frank, 2006). Twenty factors were chosen as the cutoff for the correspondence analysis of mixed orientations. Factors with six largest eigenvalues were used to assess the resolvability of orientations: Euclidian distances between any pair of clusters in the 6D space were calculated. By applying the Raileigh principle, it was decided that it was resolvable as the distance between the cluster centers is greater than the sum of the two cluster radii. The total number of distances measured was

$$\frac{20 \times 19}{1 \times 2},$$

and the percentage of resolvable pairs was counted. Similar correspondence analyses were performed over mixed conformations and mixed compositions.

## Alignment

The template set T was subjected to reference-free alignment (SPIDER operation of "AP SR"): optimal rotation and translation parameters returned by "AP SR" were applied to the corresponding image in the replica set R. An average was generated from the replica set R, aligned to the potential map. The resolution was assessed by comparing the average with the potential map by FRC analysis (SPIDER: RF) with a cutoff of 0.5 (Frank, 2006). The minimum number of particles required for 3D reconstruction was calculated by

$$N_{\min} = N_{\text{proj}} \times \pi \times D/d, \quad (23)$$

where D is the estimate of the diameter of the protein as a compact sphere and d the targeted resolution. For pol II, TIR, and T7 pol-Lys, D is 10.5 nm, 8.6 nm, 7.1 nm, respectively. Applying alignment parameters to the replica set R was designed to avoid amplification of noise incurred by correcting the envelope function or the B factor (Saad et al., 2001) and the CTF amplitude (Frank, 2006). To extract the B factor from the averaged image, Guinier analysis was used as described previously (Rosenthal and Henderson, 2003).

## SUPPLEMENTAL INFORMATION

Supplemental Information includes six figures and two tables and can be found with this article online at doi:10.1016/j.str.2009.12.001.

## ACKNOWLEDGMENTS

W.H.C. thanks F.-R. Chen of National Tsing-hua University, Y. Hwu of the Institute of Physics, Academia Sinica (AS), and F.J. Sigworth of Yale University for critical discussions. W.H.C. is indebted to Y.-Y. Chuang for help with collecting cryo-CEM images. The funding for this work came from AS and the National Science Council of Taiwan. C.-Y. Chen is supported by an AS fellowship.

Received: April 8, 2009

Revised: November 25, 2009

Accepted: December 2, 2009

Published: January 12, 2010

## REFERENCES

- Adiga, P.S., Malladi, R., Baxter, W., and Glaeser, R.M. (2004). A binary segmentation approach for boxing ribosome particles in cryo EM micrographs. *J. Struct. Biol.* 145, 142–151.
- Adrian, M., Dubochet, J., Lepault, J., and McDowell, A.W. (1984). Cryo-electron microscopy of viruses. *Nature* 308, 32–36.
- Area, E., Martín-Benito, J., Gastaminza, P., Torreira, E., Valpuesta, J.M., Carrascosa, J.L., and Ortín, J. (2004). 3D structure of the influenza virus polymerase complex: localization of subunit domains. *Proc. Natl. Acad. Sci. USA* 101, 308–313.
- Ban, N., Freeborn, B., Nissen, P., Penczek, P., Grassucci, R.A., Sweet, R., Frank, J., Moore, P.B., and Steitz, T.A. (1998). A 9 Å resolution X-ray crystallographic map of the large ribosomal subunit. *Cell* 93, 1105–1115.
- Bushnell, D.A., and Kornberg, R.D. (2003). Complete, 12-subunit RNA polymerase II at 4.1-Å resolution: implications for the initiation of transcription. *Proc. Natl. Acad. Sci. USA* 100, 6969–6973.
- Bushnell, D.A., Westover, K.D., Davis, R.E., and Kornberg, R.D. (2004). Structural basis of transcription: An RNA polymerase II-TFIIB cocystal at 4.5 Å resolution. *Science* 303, 983–988.
- Cambie, R., Downing, K.H., Typke, D., Glaeser, R.M., and Jin, J. (2007). Design of a microfabricated, two-electrode phase-contrast element suitable for electron microscopy. *Ultramicroscopy* 107, 329–339.
- Chen, C.-Y., Chang, C.-C., Yen, C.-F., Chiu, M.T.-K., and Chang, W.-H. (2009a). Mapping RNA exit channel on transcribing RNA polymerase II by FRET analysis. *Proc. Natl. Acad. Sci. USA* 106, 127–132.
- Chen, J.Z., Settembre, E.C., Aoki, S.T., Zhang, X., Bellamy, A.R., Dormitzer, P.R., Harrison, S.C., and Grigorieff, N. (2009b). Molecular interactions in rotavirus assembly and uncoating seen by high-resolution cryo-EM. *Proc. Natl. Acad. Sci. USA* 106, 10644–10648.
- Cheng, R.H., Olson, N.H., and Baker, T.S. (1992). Cauliflower mosaic virus: a 420 subunit (T=7), multilayer structure. *Virology* 186, 655–668.
- Chiu, W., and Glaeser, R.M. (1975). Single atom image contrast: conventional dark-field and bright-field electron microscopy. *J. Microsc.* 103, 33–54.
- Clare, D.K., Bakkes, P.J., van Heerikhuizen, H., van der Vies, S.M., and Saibil, H.R. (2009). Chaperonin complex with a newly folded protein encapsulated in the folding chamber. *Nature* 457, 107–110.
- Craighead, J.L., Chang, W.H., and Asturias, F.J. (2002). Structure of yeast RNA polymerase II in solution: implications for enzyme regulation and interaction with promoter DNA. *Structure* 10, 1117–1125.
- Danev, R., and Nagayama, K. (2001). Transmission electron microscopy with Zernike phase plate. *Ultramicroscopy* 88, 243–252.
- Danev, R., and Nagayama, K. (2008). Single particle analysis based on Zernike phase contrast transmission electron microscopy. *J. Struct. Biol.* 161, 211–218.
- Danev, R., Glaeser, M., and Nagayama, K. (2009). Practical factors affecting the performance of thin-film phase plate for transmission electron microscopy. *Ultramicroscopy* 109, 312–325.
- Darst, S.A., Opalka, N., Chacon, P., Polyakov, A., Richter, C., Zhang, G., and Wriggers, W. (2002). Conformational flexibility of bacterial RNA polymerase. *Proc. Natl. Acad. Sci. USA* 99, 4296–4301.
- De Carlo, S., Carles, C., Riva, M., and Schultz, P. (2003). Cryo-negative staining reveals conformational flexibility within yeast RNA polymerase I. *J. Mol. Biol.* 329, 891–902.
- Edwards, A.M., Kane, C.M., Young, R.A., and Kornberg, R.D. (1991). Two dissociable subunits of yeast RNA polymerase II stimulate the initiation of transcription at a promoter in vitro. *J. Biol. Chem.* 266, 71–75.
- Erickson, H., and Klug, A. (1971). Measurement and compensation of defocusing and aberrations by Fourier processing of electron micrographs. *Philos. Trans. R. Soc. Lond. B Biol. Sci.* 261, 106–118.
- Frank, J. (2002). Single-particle imaging of macromolecules by cryo-electron microscopy. *Annu. Rev. Biophys. Biomol. Struct.* 31, 303–319.
- Frank, J. (2006). *Three-Dimensional Electron Microscopy of Macromolecular Assemblies* (New York: Oxford University Press).

- Frank, J., Radermacher, M., Penczek, P., Zhu, J., Li, Y., Ladjadj, M., and Leith, A. (1996). SPIDER and WEB: processing and visualization of images in 3D electron microscopy and related fields. *J. Struct. Biol.* **116**, 190–199.
- Frank, J., Gao, H., Sengupta, J., Gao, N., and Taylor, D.J. (2007). The process of mRNA-tRNA translation. *Proc. Natl. Acad. Sci. USA* **104**, 19671–19678.
- Fu, J., Gnat, A.L., Bushnell, D.A., Jensen, G.J., Thompson, N.E., Burgess, R.R., David, P.R., and Kornberg, R.D. (1999). Yeast RNA polymerase II at 5 Å resolution. *Cell* **98**, 799–810.
- Fu, J., Gao, H., and Frank, J. (2007). Unsupervised classification of single particles by cluster tracking in multi-dimensional space. *J. Struct. Biol.* **157**, 226–239.
- Fultz, B., and Howe, J.M. (2005). *Transmission Electron Microscopy and Diffractometry of Materials*, Second Edition (Berlin: Springer).
- Gao, H., Valle, M., Ehrenberg, M., and Frank, J. (2004). Dynamics of EF-G interaction with the ribosome explored by classification of a heterogeneous cryo-EM dataset. *J. Struct. Biol.* **147**, 283–290.
- Gavin, A.C., Bosche, M., Krause, R., Grandi, P., Marzioch, M., Bauer, A., Schultz, J., Rick, J.M., Michon, A.M., Cruciati, C.M., et al. (2002). Functional organization of the yeast proteome by systematic analysis of protein complexes. *Nature* **415**, 141–147.
- Glaeser, R.M. (1999). Review: electron crystallography: present excitement, a nod to the past, anticipating the future. *J. Struct. Biol.* **128**, 3–14.
- Glaeser, R.M. (2004). Historical background: Why is it important to improve automated particle selection methods? *J. Struct. Biol.* **145**, 15–18.
- Gonen, T., Cheng, Y., Sliz, P., Hiroaki, Y., Fujiyoshi, Y., Harrison, S.C., and Walz, T. (2005). Lipid-protein interactions in double-layered two-dimensional AQP0 crystals. *Nature* **438**, 633–638.
- Haider, M., Muller, H., Uhlemann, S., Zach, J., Loebau, U., and Hoeschen, R. (2008). Prerequisites for a Cc/Cs-corrected ultrahigh-resolution TEM. *Ultramicroscopy* **108**, 167–178.
- Henderson, R. (1995). The potential and limitations of neutrons, electrons and X-rays for atomic resolution microscopy of unstained biological molecules. *Q. Rev. Biophys.* **28**, 171–193.
- Henderson, R., Baldwin, J.M., Ceska, T.A., Zemlin, F., Beckmann, E., and Downing, K.H. (1990). Model for the structure of bacteriorhodopsin based on high-resolution electron cryo-microscopy. *J. Mol. Biol.* **213**, 899–929.
- Huang, S.H., Wang, W.J., Chang, C.S., Hwu, Y.K., Tseng, F.G., Kai, J.J., and Chen, F.R. (2006). The fabrication and application of Zernike electrostatic phase plate. *J. Electron Microsc. (Tokyo)* **55**, 273–280.
- Jensen, G.J. (2001). Alignment error envelopes for single particle analysis. *J. Struct. Biol.* **133**, 143–155.
- Kostek, S.A., Grob, P., De Carlo, S., Lipscomb, J.S., Garczarek, F., and Nogales, E. (2006). Molecular architecture and conformational flexibility of human RNA polymerase II. *Structure* **14**, 1691–1700.
- Ludtke, S.J., and Chiu, W. (2003). Focal pair merging for contrast enhancement of single particles. *J. Struct. Biol.* **144**, 73–78.
- Ludtke, S.J., Baldwin, P.R., and Chiu, W. (1999). EMAN: semiautomated software for high-resolution single-particle reconstructions. *J. Struct. Biol.* **128**, 82–97.
- Ludtke, S.J., Chen, D.H., Song, J.L., Chuang, D.T., and Chiu, W. (2004). Seeing GroEL at 6 Å resolution by single particle electron cryomicroscopy. *Structure* **12**, 1129–1136.
- Ludtke, S.J., Baker, M.L., Chen, D.H., Song, J.L., Chuang, D.T., and Chiu, W. (2008). De novo backbone trace of GroEL from single particle electron cryomicroscopy. *Structure* **16**, 441–448.
- Majorovits, E., Barton, B., Schultheiss, K., Perez-Willard, F., Gerthsen, D., and Schroder, R.R. (2007). Optimizing phase contrast in transmission electron microscopy with an electrostatic (Boersch) phase plate. *Ultramicroscopy* **107**, 213–226.
- Malac, M., Beleggia, M., Egerton, R., and Zhu, Y. (2007). Imaging of radiation-sensitive samples in transmission electron microscopes equipped with Zernike phase plates. *Ultramicroscopy* **108**, 126–140.
- Mallick, S.P., Carragher, B., Potter, C.S., and Kriegman, D.J. (2005). ACE: automated CTF estimation. *Ultramicroscopy* **104**, 8–29.
- Rez, P. (2003). Comparison of phase contrast transmission electron microscopy with optimized scanning transmission annular dark field imaging for protein imaging. *Ultramicroscopy* **96**, 117–124.
- Rose, A. (1948). The sensitivity performance of the human eye on an absolute scale. *J. Opt. Soc. Am.* **38**, 196–208.
- Rosenthal, P.B., and Henderson, R. (2003). Optimal determination of particle orientation, absolute hand, and contrast loss in single-particle electron cryomicroscopy. *J. Mol. Biol.* **333**, 721–745.
- Saad, A., Ludtke, S.J., Jakana, J., Rixon, F.J., Tsuruta, H., and Chiu, W. (2001). Fourier amplitude decay of electron cryomicroscopic images of single particles and effects on structure determination. *J. Struct. Biol.* **133**, 32–42.
- Sali, A. (2003). NIH workshop on structural proteomics of biological complexes. *Structure* **11**, 1043–1047.
- Sander, B., Golas, M.M., and Stark, H. (2003). Automatic CTF correction for single particles based upon multivariate statistical analysis of individual power spectra. *J. Struct. Biol.* **142**, 392–401.
- Scheres, S.H.W., Gao, H., Valle, M., Herman, G.T., Eggermont, P.P.B., Joachim Frank, J., and Carazo, J.-M. (2007a). Disentangling conformational states of macromolecules in 3D-EM through likelihood optimization. *Nat. Methods* **4**, 27–29.
- Scheres, S.H.W., Núñez-Ramírez, R., Gómez-Llorente, Y., San Martín, C., Eggermont, P.P.B., and Carazo, J.-M. (2007b). Modeling experimental image formation for likelihood-based classification of electron microscopy data. *Structure* **15**, 1167–1177.
- Scheres, S.H.W., Valle, M., Grob, P., Nogales, E., and Carazo, J.M. (2009). Maximum likelihood refinement of electron microscopy data with normalization errors. *J. Struct. Biol.* **166**, 234–240.
- Schultheiß, K., Pérez-Willard, F., Barton, B., Gerthsen, D., and Schröder, R.R. (2006). Fabrication of a Boersch phase plate for phase contrast imaging in a transmission electron microscope. *Rev. Sci. Instrum.* **77**, 33701–33704.
- Shiue, J., Chang, C.S., Huang, S.H., Hsu, C.H., Tsai, J.S., Chang, W.H., Wu, Y.M., Lin, Y.C., Kuo, P.C., Huang, Y.S., et al. (2009). Phase TEM for biological imaging utilizing a Boersch electrostatic phase plate: theory and practice. *J. Electron Microsc. (Tokyo)* **58**, 137–145.
- Stagg, S.M., Lander, G.C., Pulokas, J., Fellmann, D., Cheng, A., Quispe, J.D., Mallick, S.P., Avila, R.M., Carragher, B., and Potter, C.S. (2006). Automated cryoEM data acquisition and analysis of 284742 particles of GroEL. *J. Struct. Biol.* **155**, 470–481.
- Stark, H., Dube, P., Luhrmann, R., and Kastner, B. (2001). Arrangement of RNA and proteins in the spliceosomal U1 small nuclear ribonucleoprotein particle. *Nature* **409**, 539–542.
- Sugitani, S., and Nagayama, K. (2002). Complex observation in electron microscopy: III. Inverse theory of observation-scheme dependent information transfer. *Journal of the Physical Society of Japan* **71**, 744–756.
- Taylor, K.A., and Glaeser, R.M. (1974). Electron diffraction of frozen, hydrated protein crystals. *Science* **186**, 1036–1037.
- Thon, F. (1966). Zur Defokussierungsabhängigkeit des Phasenkontrastes bei der elektronenmikroskopischen Abbildung. *Zeitschrift für Naturforschung* **21a**, 476–478.
- Unwin, N. (2005). Refined structure of the nicotinic acetylcholine receptor at 4 Å resolution. *J. Mol. Biol.* **346**, 967–989.
- van Heel, M., Gowen, B., Matadeen, R., Orlova, E.V., Finn, R., Pape, T., Cohen, D., Stark, H., Schmidt, R., Schatz, M., and Patwardhan, A. (2000). Single-particle electron cryo-microscopy: towards atomic resolution. *Q. Rev. Biophys.* **33**, 307–369.
- Wang, L., Bose, P.S., and Sigworth, F.J. (2006). Using cryo-EM to measure the dipole potential of a lipid membrane. *Proc. Natl. Acad. Sci. USA* **103**, 18528–18533.
- Yonekura, K., Maki-Yonekura, S., and Namba, K. (2003). Complete atomic model of the bacterial flagellar filament by electron cryomicroscopy. *Nature* **424**, 643–650.
- Zernike, F. (1955). How I discovered phase contrast. *Science* **121**, 345–349.
- Zhou, Z.H., Hardt, S., Wang, B., Sherman, M.B., Jakana, J., and Chiu, W. (1996). CTF determination of images of ice-embedded single particles using a graphics interface. *J. Struct. Biol.* **116**, 216–222.